



Nonlinear aspects of focusing internal waves

Natalia D. Shmakova^{1,2} and Jan-Bert Flór^{1,†}

¹Laboratoire des Écoulements Géophysiques et Industriels (LEGI), CNRS–Université Grenoble Alpes, F38000, Grenoble, France

²Lavrentyev Institute of Hydrodynamics, Siberian Branch of the Russian Academy of Sciences, Prospekt Lavrentyev 15, Novosibirsk 630090, Russia

(Received 12 October 2018; revised 14 December 2018; accepted 14 December 2018; first published online 11 January 2019)

When a torus oscillates horizontally in a linearly stratified fluid, the wave rays form a double cone, one upward and one downward, with two focal points where the wave amplitude has a maximum due to wave focusing. Following a former study on linear aspects of wave focusing (Ermanyuk *et al.*, *J. Fluid Mech.*, vol. 813, 2017, pp. 695–715), we here consider experimental results on the nonlinear aspects that occur in the focal region below the torus for higher-amplitude forcing. A new non-dimensional number that is based on heuristic arguments for the wave amplitude in the focal area is presented. This focusing number is defined as $Fo = (A/a)\epsilon^{-1/2}f(\theta)$, with oscillation amplitude A , $f(\theta)$ a function for the variation of the wave amplitude with wave angle θ , and $\epsilon^{1/2} = \sqrt{b/a}$ the increase in amplitude due to the focusing, with a and b , respectively, the minor and major radius of the torus. Nonlinear effects occur for $Fo \geq 0.1$, with the shear stress giving rise to a mean flow which results in the focal region in a central upward motion partially surrounded by a downward motion. With increasing Fo , the Richardson number Ri measured from the wave steepness monotonically decreases. Wave breaking occurs at $Fo \approx 0.23$, corresponding to $Ri = 0.25$. In this regime, the focal region is unstable due to triadic wave resonance. For the different tori sizes under consideration, the triadic resonant instability in these three-dimensional flows resembles closely the resonance observed by Bourget *et al.* (*J. Fluid Mech.*, vol. 723, 2013, pp. 1–20) for a two-dimensional flow, with only minor differences. Application to internal tidal waves in the ocean are discussed.

Key words: internal waves, mixing and dispersion, stratified flows

1. Introduction

In view of its relevance to the tidal motion over topography in the oceans, internal wave radiation in stratified and rotating fluids has been investigated in detail for oscillating objects such as cylinders and spheres (see, for example, Flynn, Onu

† Email address for correspondence: flor@legi.cnrs.fr

& Sutherland 2003; Onu, Flynn & Sutherland 2003; Voisin 2003; King, Zhang & Swinney 2009; Voisin, Ermanyuk & Flór 2011). Internal waves were mainly found to diverge, away from the source region, and thus to decrease in energy. The oscillation of horizontally curved objects causes, due to the convergence of wave beams, a well-distinguishable focusing effect (Bühler & Muller 2007; Duran-Matute *et al.* 2013; Ermanyuk, Shmakova & Flór 2017). By conservation of momentum, the wave energy density increases with distance from the location of generation, since the wave beam cross-section decreases, thus causing an increase in amplitude. In situ observations in ocean canyons and straits (Buijsman, Legg & Klymak 2012; Vlasenko *et al.* 2016) and curved mountains or craters (Peliz, Le Cann & Mohn 2009; Dale & Inall 2015) do show a high increase in internal wave amplitude. The ocean inside a deep submerged crater with a torus shape close to Portugal is found to be entirely mixed (Peliz *et al.* 2009). These observations suggest that overturning due to wave focusing may be a potential candidate for local mixing processes in the oceans.

Theoretical considerations for a ring-shaped torus with Gaussian generatrix (Bühler & Muller 2007) suggest an amplitude amplification in the focal zone proportional to the square root of the torus aspect ratio, as is confirmed by experiments and energy arguments for a horizontally oscillating torus with a circular generatrix by Ermanyuk *et al.* (2017). In the present study, for low and moderate oscillation amplitudes, the focusing amplifies the internal wave amplitude almost two times in the focal zone, implying for a same wavelength a comparable increase in shear and isopycnal slopes. For a torus of aspect ratio $\epsilon = 5$ and oscillation amplitude A , the waves in the focal region were shown to be linear for $Ke < 0.4$, with $Ke = A/a$ the Keulegan–Carpenter number, and were compared successfully with the linear theory adapted from Hurley & Keady (1997). When increasing the oscillation amplitude, nonlinear effects started at $Ke \approx 0.6$ and breaking occurred for $Ke > 0.8$, mainly in the focal region and far away from the oscillating object. Experimental and numerical investigation of inertial wave focusing in rotating fluids showed for very high amplitudes of oscillation the existence of wave-induced turbulence in the focal zone (Duran-Matute *et al.* 2013), which was used to study the effects of rotation on turbulence in isolation.

Here, we concentrate on the nonlinear aspects of wave focusing. The streaming instability that causes a mean flow and the triadic resonant instabilities, giving rise to the presence of lower harmonics, have recently been reviewed by Dauxois *et al.* (2018). For a uniform two-dimensional wave beam, Bourget *et al.* (2013) showed the presence of the triadic resonant instability, where in contrast to the parametric subharmonic instability, the resonant frequencies of the triad are not equal to half the dominant wave frequency. Dauxois *et al.* (2018) stress the relevance of three dimensional and finite-width beam effects. Recent theoretical investigations by Kataoka & Akylas (2016) and Fan, Kataoka & Akylas (2018) discuss the instability of two wave beams which are unstable in three dimensions when they are separated, and/or have different angles of propagation. In the present study on focusing wave beams, the wave frequencies are equal, but due to the geometry of the focusing, wave beams are not parallel. The Reynolds stress increases towards the focal point and enhances a mean flow in the focal region. For high amplitudes, a triadic resonant instability generating two secondary waves of different frequencies and wavelengths is observed near the focal region. We discuss the effects of focusing on the mean flow generation and the observed triadic resonance.

The paper is organised as follows. Section 2 describes the experimental set-up and data processing methods, § 3 introduces the new non-dimensional focusing number and its relation to the Richardson number followed by the description of the focusing flow and mean flow towards the focal region in § 4. The resonant triadic wave interaction is reported in § 5, and the results are summarised and further discussed in § 6.

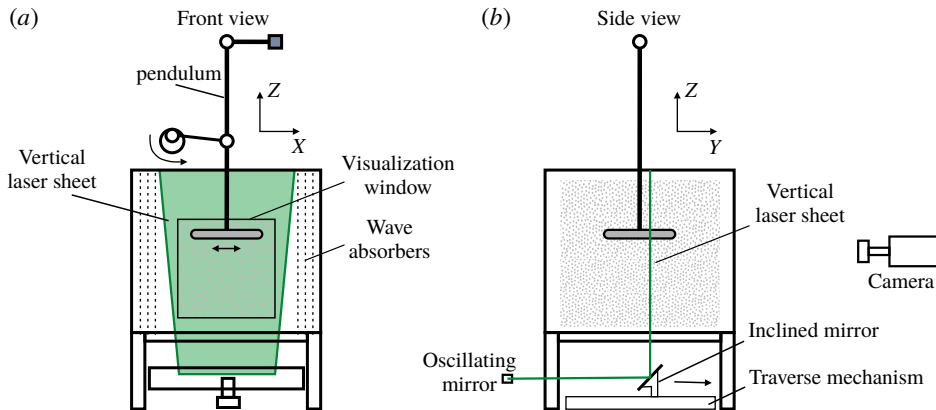


FIGURE 1. Sketch of the experimental set-up: (a) front view and (b) side view with the seeded particles as light grey dots and the laser plane shown in green.

2. Experimental set-up and data processing

Experiments were carried out in a Plexiglas cubic tank of dimensions $97 \times 97 \times 97$ cm³ filled with a 85 cm deep linearly salt-stratified fluid. Internal waves were generated by horizontal oscillations of amplitude A of a Plexiglas torus of minor radius $a = 1, 1.5$ or 2 cm and major radius $b = 34, 13.5$ or 10 cm, respectively. The aspect ratio, defined as $\epsilon = b/a$, thus has values of $34, 9$ or 5 , respectively. To avoid wave reflections, the two side-walls of the tank perpendicular to the direction of oscillation were covered with a mesh of wave absorbers of 5 cm thickness (see figure 1).

The stratification was established with the standard double-bucket technique. The density was measured at different heights in the fluid with an Anton Paar densimeter. From these values the density profile was calculated, providing the buoyancy frequency $N = [(-g/\rho)d\rho/dz]^{1/2}$, with g the gravitational acceleration and $\rho(z)$ the density distribution over the vertical coordinate z . The values of N are presented in table 1.

To measure the flow in the vertical plane of symmetry $Y = 0$, the particle image velocimetry (PIV) method or the planar laser induced fluorescence (P-LIF) method was used. For the latter method, a grid of horizontally spanned cotton wires, painted with fluorescein dye, was dragged carefully through the fluid to generate a set of approximately 1 mm thick and equidistant horizontal dye planes before the experiment. These dye planes were illuminated by a vertical laser sheet. Diffusion of the dye gives a Gaussian distribution which, with subpixel resolution, allows for a very accurate localisation of the maximum, and therefore precise measurement of the wave motion (see Voisin *et al.* 2011). For the PIV measurements, prior to the experiment, the fluid was seeded with 60 μm Orgasol[®] particles of density $\rho = 1.02$ kg m⁻³, which were illuminated with a vertical laser sheet through the torus centre (see figure 1). Images were taken by a 12-bit Dalsa camera with a charge-coupled device (CCD) of 1024×1024 pixels. The particle displacement was obtained by cross-correlating two successive images using standard PIV techniques, and in particular, the UVMAT/CIVx software packages developed at LEGI providing the vertical $w(t)$ and longitudinal horizontal $u(t)$ velocities. (<http://www.legi.cnrs.fr/web/spip.php?article763&lang=en>.) In some experiments, the LIF technique that is described in detail in Voisin

Exp	Method	ϵ	Ke (Fo)	ω/N	N (rad s ⁻¹)	Z	Z_{focal}
A	LIF and PIV	34	0.35; 0.75; 1.0; 1.3; 1.6 (0.036; 0.076; 0.10; 0.13; 0.16)	0.79	0.75	0 to -70	-45
B	LIF	9	0.19; 0.41; 0.65; 0.84; 1.1 (0.039; 0.08; 0.13; 0.17; 0.23)	0.80	0.72	-1.84 to -21.8	-11.2
C	PIV	9	0.21; 0.57; 0.78; 1.06; 1.26 (0.043; 0.12; 0.16; 0.22; 0.26)	0.80	0.83	-1 to -16.75	-7.8
D	LIF	5	0.15; 0.3; 0.52; 0.72 (0.036; 0.08; 0.14; 0.20)	0.81	0.72	-1.88 to -16.88	-5.5
E	PIV	5	0.19; 0.41; 0.6; 0.95; 1.2 (0.053; 0.11; 0.16; 0.26; 0.33)	0.80	0.83	-1 to -10.88	-4.7

TABLE 1. Experimental parameters and measurement methods used, with $\epsilon = b/a$ the torus aspect ratio, $Ke = A/a$ the Keulegan–Carpenter number and ω/N the non-dimensional oscillation frequency. Z is the measured region and Z_{focal} corresponds to the geometrical point of intersection of the wave rays, both non-dimensionalized with a . The focusing wave number Fo is defined in § 3. Experiments B–E are also used in Ermanyuk *et al.* (2017).

et al. (2011), Ermanyuk, Flór & Voisin (2011) was used (see table 1), and allowed calculation of the isopycnal slopes from the vertical displacement ζ as $S(t) = \arctan(\Delta\zeta/\Delta x)$ with a very high resolution, since it provided a continuous and sub-pixel signal in space. Below we are using the maximum isopycnal slope S^* obtained for each LIF experiment in the focal region. To select the different wave modes and distinguish their propagation direction, the Hilbert transform method of Mercier, Garnier & Dauxois (2008) was used.

To locate the measurement results in space, in the following we define a Cartesian coordinate system with the origin at the centre of the torus at rest, the z -axis pointing vertically upwards, and horizontal axis x and y respectively along and perpendicular to the direction of oscillation. These coordinates have been non-dimensionalised with the minor radius a , so that $(X, Y, Z) = (x, y, z)/a$, whereas the velocity components are normalised as $(U, V, W) = (u, v, w)/(A\omega)$, with ω the oscillation frequency. In table 1 the experimental parameters are presented.

3. Focusing number

To characterise the generation of internal waves by an oscillating obstacle, the non-dimensional oscillation frequency ω/N and the Keulegan–Carpenter number, $Ke = A/a$ with A the oscillation amplitude are generally used. The variation of the maximum waveslope as a function of Ke is presented in figure 2(a) for tori with $\epsilon = 5, 9$ and 34, with each torus aspect ratio causing a different relation between isopycnal slope and excitation amplitude. This number is based on the maximum vertical displacement relative to the size of the object, and characterizes the wave amplitude close to the torus where the effects of curvature are hardly detectable. At large distances from the torus, however, the geometric effect of focusing causes a much larger wave amplitude. Thus each torus causes a different amplitude in the focal region (see figure 2a). To uniformly predict the amplitude in the focal region, the length scale of the torus radius b needs to be incorporated. The wave motion due to the fluid displacement of each

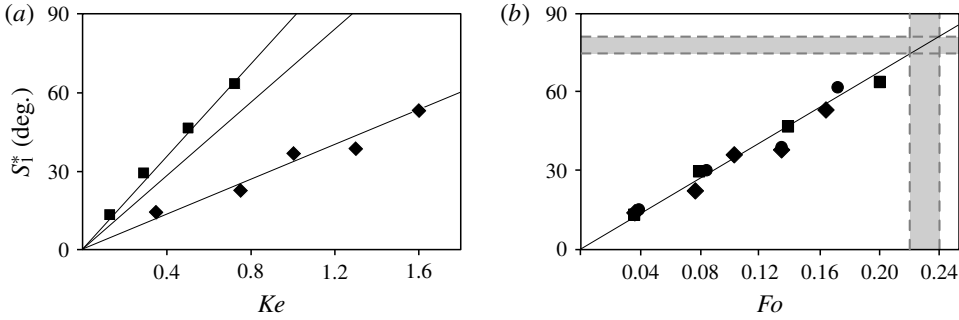


FIGURE 2. Maximum isopycnal slope attained during one period, against (a) Ke and (b) Fo numbers, with squares for the torus of $\epsilon = 5$ at $Z = -6$ (Exp. D), circles for the torus of $\epsilon = 9$ at $Z = -11.2$ (Exp. B) and diamonds for the torus of $\epsilon = 34$ at $Z = -45$ (Exp. A). The error in the measurements is smaller than the size of the dots. The vertical grey area in (b) represents the critical focusing number $Fo = 0.23 \pm 0.01$ for overturning (see text) and the horizontal grey area the corresponding angle in isopycnal wave slope $78 \pm 3^\circ$. Experimental parameters are presented in table 1.

segment of the torus is accumulated in the focal region. When integrated over the radius of the torus, this implies the additional length scale of the torus radius, b . The length scale we propose is the geometric mean \sqrt{ab} , also related to the surface of the torus $\pi^2 ab$, providing the adapted Keulegan–Carpenter number

$$Ke' = \frac{A}{\sqrt{ab}} = \frac{A/\epsilon^{1/2}}{a}. \tag{3.1}$$

The value $\epsilon^{1/2} = (b/a)^{1/2}$ turns out to be the amplification of the amplitude in the focal region, and is also obtained from the energy estimations of the vertical displacement in the focal region of a torus (Ermanyuk *et al.* 2017) and Gaussian-shaped torus (Bühler & Muller 2007).

Since the wave amplitude varies significantly with the oscillation frequency (see Voisin *et al.* 2011), we also take into account this variation. Multiplying the wave amplitude with this factor (see Voisin *et al.* 2011), we obtain what we will further call the focusing number

$$Fo = \frac{A}{a} \epsilon^{-1/2} \sin^{1/2} \theta \cos \theta. \tag{3.2}$$

For $\omega = 0$ and $\omega = N$, the focusing effect tends to zero, and it is maximal for $\theta = 35^\circ$.

The evolution of the maximum isopycnal slope against Fo is presented in figure 2(b). All three tori with $\epsilon = 5, 9$ and 34 collapse on one line. This result suggests the focusing number as an appropriate non-dimensional parameter for converging waves. Below, we focus on the breaking in the focal region.

3.1. Richardson and focusing numbers

In order to find the critical values of the focusing number for breaking, we plot the Richardson number as a function of the focusing number. In the linear approximation

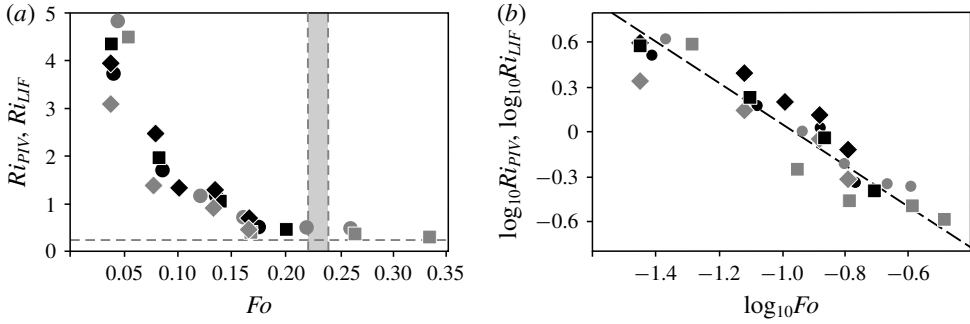


FIGURE 3. Richardson numbers Ri_{PIV} from PIV data (grey symbols) for experiments Exp. C (circles), Exp. E (squares) and Exp. A (diamonds), and Ri_{LIF} from LIF data (black symbols) for experiments Exp. B (circles), Exp. D (squares) and Exp. A (diamonds) with parameters given in table 1 in (a) a linear and (b) a logarithmic representation. The vertical grey lines denote the value of Fo corresponding to the onset of overturning. The black dashed line in (b) represents the average trend of the data.

the vorticity equation for internal waves can be represented by a balance with the baroclinic torque given by

$$\frac{\partial \omega_y}{\partial t} = \left(\frac{\nabla p \times \nabla \rho}{\rho^2} \right)_y = \frac{1}{\rho^2} \left(\frac{\partial p}{\partial z} \frac{\partial \rho}{\partial x} - \frac{\partial p}{\partial x} \frac{\partial \rho}{\partial z} \right) \approx -\frac{g}{\rho} \frac{\partial \rho}{\partial x}, \quad (3.3)$$

where for the latter equality the Boussinesq approximation is used. Considering the ratio between stratification and the shear, here represented by the baroclinic torque, one obtains for the Richardson number

$$Ri_{LIF} = N^2 \left(\frac{\nabla p \times \nabla \rho}{\rho^2} \right)_y^{-1} \approx \frac{N^2}{-\frac{g}{\rho} \frac{\partial \rho}{\partial x}} = \frac{\Delta x}{\Delta z} \Big|_{\rho} = \frac{1}{\tan S}. \quad (3.4)$$

From the steepness $\Delta x/\Delta z$ of the P-LIF dye-lines the Richardson number could be measured accurately because of the sub-pixel resolution obtained with the Gaussian dye distribution mentioned above. In addition, the Richardson number in the focal region was calculated as $Ri_{PIV} = N^2/(\partial u/\partial z)^2 \approx N^2/(\Delta u/\Delta z)^2$, with N the stratification measured prior to the experiment and the variation in velocity Δu measured from the PIV data over a typical grid distance of $\Delta z = 4$ pixels corresponding to ≈ 0.15 cm. The values of this number are displayed in grey in figure 3(a) and in a log–log form in figure 3(b), and show that the values for both Richardson numbers, Ri_{PIV} and Ri_{LIF} , collapse on one curve.

Nonlinear effects, such as the generation of a mean flow and evanescent second harmonics were noticed around a value of $Fo \approx 0.1$, corresponding to $Ri \approx 1.5$. The asymptotic limit of $Ri \approx 0.25$, corresponds to overturning in stratified shear flows (see Miles 1961). The empirical relation between the Focusing number and the Richardson number can be estimated with the least-squares approximation as (see figure 3)

$$Fo = (9 \pm 0.5) Ri^{-2/3}, \quad (3.5)$$

and allows one to predict the breaking in focal regions for $Fo > 0.23 \pm 0.01$ as a function of the initial forcing parameters a, b, A and the oscillation frequency given by θ . Applying this focusing number estimation on figure 2(b) one obtains the isopycnal slope $78 \pm 3^\circ$ for breaking waves.

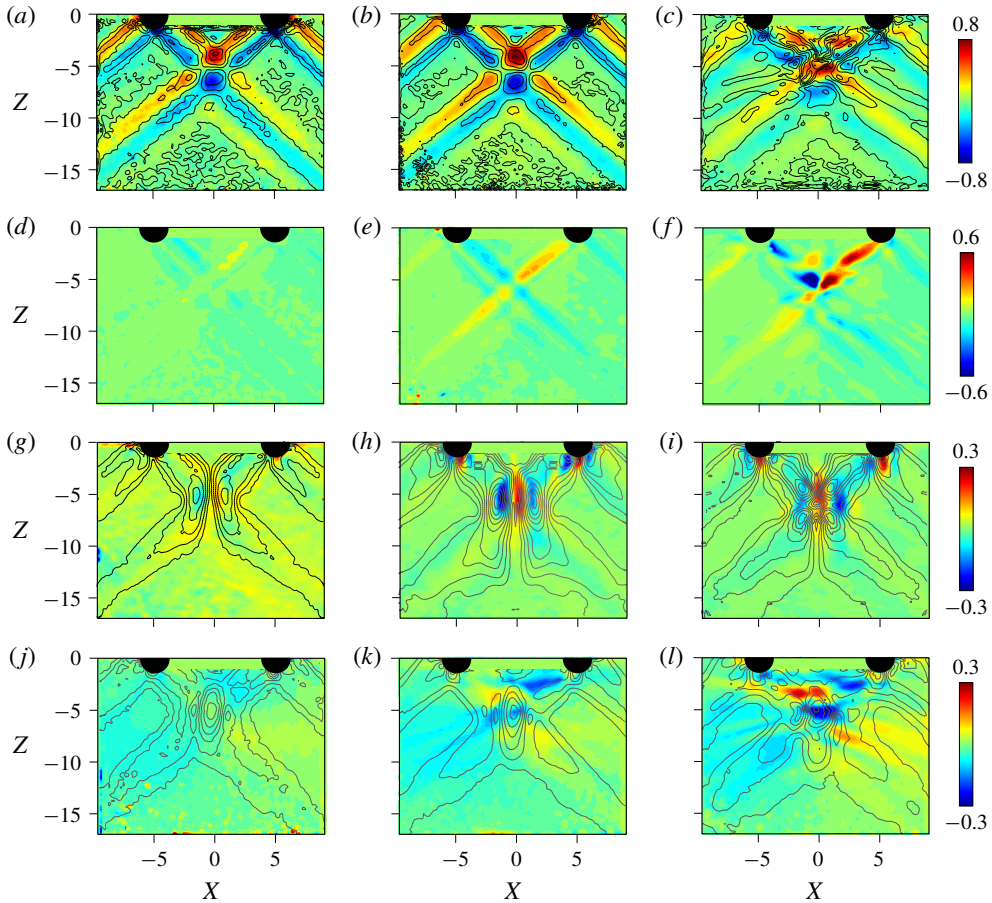


FIGURE 4. Flow variation in the vertical plane of symmetry, in the steady regime after 20 oscillation periods with (a,d,g,j) $Fo = 0.053$, (b,e,h,k) $Fo = 0.16$, and (c,f,i,l) $Fo = 0.33$; (a–c) instantaneous profiles of the horizontal velocity U (colour) and contours of the horizontal transverse vorticity at phase $\pi/2$ (rightmost torus position); (d–f) shear stress $\overline{U'W'}$; (g–i) vertical mean flow W_0 and (j–l) horizontal mean flow U_0 . The mean flow and shear stress are averaged over one period of oscillation. In images (g–l), the contours indicate the velocity amplitude. Exp. E from table 1.

4. Observations

Figure 4(a–c) shows the change in the instantaneous horizontal velocity of the wave pattern in the vertical plane of symmetry $Y = 0$ for increasing values of Fo . One-half period later the direction of the velocity is reversed, implying a standing wave motion in the focal zone. The temporal motion in the focal region is therefore oscillatory, like a standing wave. This wave motion consists of the first harmonic, with all higher harmonics being evanescent since $\omega/N > 0.5$, the wave structure having the same dipolar shape as that observed for spherical objects in Shmakova, Ermanyuk & Flór (2017). The amplitude of the converging waves remains approximately constant. With increasing Fo number from 0.053 to 0.16 (in respectively figures 4a, 4b), a clear increase in wave amplitude can be noticed. The vorticity contours coincide with the

wave contours as long as wave breaking is absent, as shown in figure 4(a,b), while for $Fo = 0.33$ in figure 4(c), the vorticity contours reveal the presence of breaking wave structures.

Figure 4(d-f) shows the non-dimensional shear stress, $\overline{U'W'}$, averaged over one period. In the linear regime ($Fo < 0.1$, see figure 4d), it is negligible for the outward moving (diverging) wave beams but is nonzero for the converging (focusing) wave beams, suggesting that the conical geometry of the focusing wave has a direct effect on the shear stress also. Since the wave amplitude in the focusing wave beam increases, intrinsically also U' and W' increase, giving rise to larger shear stress (see figure 4e).

It is its gradient that is responsible for the mean flow towards the focal region (Fan *et al.* 2018), leading to a strong vertical motion there, as shown in figure 4(h). Viscous dissipation towards the focal region, which is an essential ingredient for the streaming instability (see Fan *et al.* 2018), is, however, overtaken by the effect of focusing. In the fully nonlinear regime, for $Fo > 0.23$, due to wave breaking the beam loses its coherence, and its direction is locally bent due to nonlinear interactions with the waves (figure 4f).

The mean flow is shown in figure 4(g-i) for the $Y=0$ -symmetry plane. In the linear regime $Fo < 0.1$, it is small but non-negligible with very small amplitudes $O(0.06)$ for the mean vertical velocity. In the nonlinear regime $Fo > 0.1$, the motion in the focal region resembles a plume motion (see figure 4g-i). Since the torus is oscillating horizontally there is, however, no axial symmetry, but the amplitude decreases away from the mid-plane $Y=0$ (see Ermanyuk *et al.* 2017).

When breaking occurs for $Fo > 0.23$ (figure 4c,f,i,l) the structure in the mean vertical and mean horizontal velocities remain clearly distinguishable, but the temporal horizontal motion (see figure 4c) is affected by breaking as well as the presence of the wave triads that are discussed further below.

5. Triadic resonance and breaking in the focal zone

Patterns of the horizontal velocity U (figure 4a-c) show that for small Fo values, the focal zone is represented by a standing wave. For large $Fo > 0.23$, new internal waves are generated, which are subharmonics, as their lower angle of propagation reveals. The time-frequency spectrum for the energy was obtained from vertical and horizontal components of the velocity $E_{uv} = (u^2 + v^2)/2$ defined by

$$Q_{E_{uv}}(t, \omega) = \left\langle \left| \int_{-\infty}^{+\infty} d\tau E_{uv}(\tau) \exp^{-i\omega\tau} h(t - \tau) \right|^2 \right\rangle_{xz}, \quad (5.1)$$

where $h(t)$ is a Hamming window, and the average is taken over an interrogation area xz around the focal region (Flandrin 1998). The corresponding energy spectrum for $Fo = 0.33$ is presented in figure 5, and shows clearly the generation of the first harmonic and two subharmonics, which satisfy

$$\omega^0 = \omega^1 + \omega^2, \quad (5.2)$$

with ω^0 the frequency of the first harmonic, and ω^1 and ω^2 the frequencies of first and second subharmonics, respectively. Using the Hilbert transform method of Mercier *et al.* (2008), the signal was filtered around a certain frequency in time for each harmonic (see figure 6a-c), and then, to obtain the phase propagation, filtered for the

Nonlinear aspects of focusing internal waves

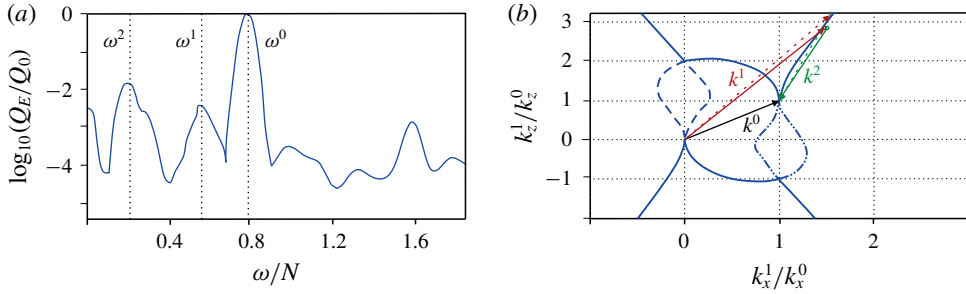


FIGURE 5. (a) Energy spectrum $\log_{10}(Q_{E_{uw}}(t, \omega)/Q_0)$ for the wave energy E_{uw} with the non-dimensional frequency ω/N averaged over five periods of oscillations after reaching the steady regime for the thick ($\epsilon = 5$) torus with $Fo = 0.33$. Here, Q is defined by (5.1) and $Q_0 = \max[Q_{E_{uw}}(t, \omega^0)]$. The positions of the first harmonic (ω^0) and two subharmonics ($\omega^{1,2}$) are shown with vertical dashed lines. (b) Resonance in wave-vector space (solid line) as calculated for a two-dimensional flow (see Bourget *et al.* 2013). The scaled vectors are $k_x^1/k_x^0 = 1.53$, $k_z^1/k_z^0 = 2.95$ (red); $k_x^2/k_x^0 = -0.57$, $k_z^2/k_z^0 = -1.95$ (green); and black for the scaled vector k^0 . Measurements of Exp. E (lines) and for Exp. C (dashed).

direction shown in figure 6(d–f). In figure 6 we consider the positive direction of the first harmonic and subharmonic waves, and the negative direction of the second subharmonic of the triad. The standing wave motion, generated in the focal zone by the two opposite moving waves, is thus not visible. The first harmonic with frequency $\omega/N = 0.8$ and algebraic amplitude of wave vector $k > 0$ in figure 6(a) shows an increasing amplitude towards the focal region, a local decrease in the zone of nonlinear interaction, and a decrease afterwards. Both subharmonic waves are generated in the focal zone, with the first subharmonic moving downwards ($k_z > 0$) and the second subharmonic moving upwards ($k_z < 0$) with frequencies of $\omega/N = 0.6$ and $\omega/N = 0.2$, respectively. In contrast to the subharmonic wave with $\omega/N = 0.6$, the structure of the second subharmonic ($\omega/N = 0.2$) in figure 6(c) is confined to the breaking wave region shown in the instantaneous and the average horizontal velocities of figures 4(c) and 4(l), respectively, thus suggesting a strong interaction with the wave breaking. These first harmonic and subharmonic waves form together a triadic resonance, satisfying the condition

$$k^1 + k^2 = k^0, \tag{5.3}$$

where $(k_x^1 + k_x^2)/k_x^0 = 0.96 \pm 0.04$ and $(k_z^1 + k_z^2)/k_z^0 = 1.01 \pm 0.01$, with k_x and k_z selected from the space spectrum. This triadic resonance was found in all experiments for values of $Fo > 0.23$. Even though this flow differs from former studies in being fully three-dimensional and in that the waves focus, the triad interaction in wave-vector space in figure 5(b) shows a striking resemblance with figure 5 of Bourget *et al.* (2013) for the triadic resonant instability in a flow that was in good approximation two-dimensional. Also the accuracy of the selected wave vectors is comparable to that in Brouzet *et al.* (2016). Increasing the curvature, and therewith the three-dimensionality of the flow by taking a smaller torus (i.e. smaller b) of larger cross-section (thickness a), did not change the result, as shown for $\epsilon = 5$ and $\epsilon = 9$ in figure 5.

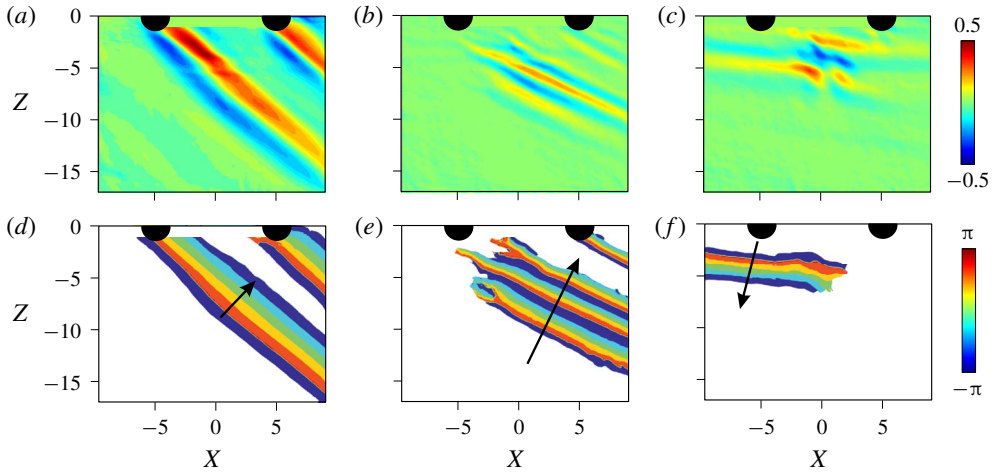


FIGURE 6. Hilbert decomposition in time and space of instantaneous horizontal velocity profile (*a–c*) and phase velocity (*d–f*) for $Fo = 0.33$. (*a,d*) First harmonic U^1 with frequency $\omega^1/N = 0.8$ and $k_z > 0$; subharmonics with (*b,e*) $\omega_1/N = 0.6$, $k_z > 0$, and (*c,f*) $\omega_2/N = 0.2$, $k_z < 0$. (Exp. E from table 1).

6. Conclusions and discussion

To characterise focusing wave fields, the number Fo has been introduced, indicating a linear regime for $Fo < 0.1$, a non-linear regime for $Fo > 0.1$, and wave breaking in the focal region for values larger than $Fo \approx 0.23$. This wave breaking occurs at an isopycnal slope of $78 \pm 3^\circ$, in agreement with observations of Ermanyuk *et al.* (2017) and corresponding to a value of the Richardson number of $Ri = 0.25$ for shear instability, and coincides with the presence of triadic resonance. In wave-vector space, this triad is very similar to the triad found by Bourget *et al.* (2013). Indeed, the present flow with the maximum amplitude in the symmetry plane $Y = 0$ (see Ermanyuk *et al.* 2017) is similar to the two-dimensional flow of Bourget *et al.* (2013), which is limited by viscous boundaries. These results suggest that the three-dimensional effects due to the curvature of the wave generator, and consequent focusing, have little qualitative effect on the triadic resonant instability. However, the wave focusing plays an important role by creating a high energy density in the focal region, thereby providing a necessary condition for the onset of the instability.

The focusing number allows for an estimation of the onset of breaking in real flows. For a typical Keulegan–Carpenter number of $Ke = 0.1$ in the ocean we can calculate the value of $\epsilon^{1/2}$ needed to reach the critical focusing number $Fo = 0.23$. For 12 hours M_2 tidal oscillation-frequency ω_{M_2} , and typical ocean stratification $N \approx \omega/0.3$, we obtain with (3.2) a value for $\epsilon^{1/2}$ of approximately 4.6, implying a major radius roughly 22 times larger than the minor radius. For large mountains, there may not be a continuity in curvature, and the focal point may be reached after reflection at the surface. But for an internal wave amplitude of 50 m and a mountain of 500 m width, this implies a large radius of 11 km indicating that focusing can cause wave breaking locally in specific places in the ocean, such as the craters mentioned in the introduction.

Acknowledgements

The authors acknowledge the helpful and constructive comments of anonymous referees, E. Ermanyuk and B. Voisin for helpful discussions, and M. Mercier for his help with the Hilbert transform method, S. Mercier and J.-M. Barnoud for technical help with the experimental setup. N.D.S. acknowledges the University of Grenoble Alpes (UGA) for funding her thesis, integration project SB RAS II.1 and RFBR 18-01-00648 for partial financial support to visit the LEGI, J.-B.F. acknowledges funding of the LabEx OSUG@2020 (Investissements d'avenir ANR10LABX56) for equipment.

References

- BOURGET, B., DAUXOIS, T., JOUBAUD, S. & ODIER, P. 2013 Experimental study of parametric subharmonic instability for internal plane waves. *J. Fluid Mech.* **723**, 1–20.
- BROUZET, C., SIBGATULLIN, I. N., SCOLAN, H., ERMANYUK, E. V. & DAUXOIS, T. 2016 Internal wave attractors examined using laboratory experiments and 3d numerical simulations. *J. Fluid Mech.* **793**, 109–131.
- BÜHLER, O. & MULLER, C. J. 2007 Instability and focusing of internal tides in the deep ocean. *J. Fluid Mech.* **588**, 1–28.
- BUIJSMAN, M. C., LEGG, S. & KLYMAK, J. 2012 Double-ridge internal tide interference and its effect on dissipation in Luzon Strait. *J. Phys. Oceanogr.* **42**, 1337–1356.
- DALE, A. C. & INALL, M. E. 2015 Tidal mixing processes amid small-scale, deep-ocean topography. *Geophys. Res. Lett.* **42**, 484–491.
- DAUXOIS, T., JOUBAUD, S., ODIER, P. & VENAILLE, A. 2018 Instabilities of internal gravity wave beams. *Ann. Rev. Fluid Mech.* **50**, 131–156.
- DURAN-MATUTE, M., FLÓR, J.-B., GODEFERD, F. S. & JAUSE-LABERT, C. 2013 Turbulence and columnar vortex formation through inertial-wave focusing. *Phys. Rev. E* **87**, 041001(R).
- ERMANYUK, E. V., FLÓR, J.-B. & VOISIN, B. 2011 Spatial structure of first and higher harmonic internal waves from a horizontally oscillating sphere. *J. Fluid Mech.* **671**, 364–383.
- ERMANYUK, E. V., SHMAKOVA, N. D. & FLÓR, J.-B. 2017 Internal wave focusing by a horizontally oscillating torus. *J. Fluid Mech.* **813**, 695–715.
- FAN, B., KATAOKA, T. & AKYLAS, T. R. 2018 On the interaction of an internal wavepacket with its induced mean flow and the role of streaming. *J. Fluid Mech.* **838**, R1.
- FLANDRIN, P. 1998 *Time–Frequency/Time–Scale Analysis*. Academic Press.
- FLYNN, M. R., ONU, K. & SUTHERLAND, B. R. 2003 Internal wave excitation by a vertically oscillating sphere. *J. Fluid Mech.* **494**, 65–93.
- HURLEY, D. G. & KEADY, G. 1997 The generation of internal waves by vibrating elliptic cylinders. Part 2. Approximate viscous solution. *J. Fluid Mech.* **351**, 119–138.
- KATAOKA, T. & AKYLAS, T. R. 2016 Three-dimensional instability of internal gravity wave beams. *Proc. International Symposium on Stratified Flows, 8th, 29 August–1 September, San Diego*. University of California San Diego.
- KING, B., ZHANG, H. P. & SWINNEY, H. L. 2009 Tidal flow over three-dimensional topography in a stratified fluid. *Phys. Fluids* **21**, 116601.
- MERCIER, M. J., GARNIER, N. B. & DAUXOIS, T. 2008 Reflection and diffraction of internal waves analyzed with the Hilbert transform. *Phys. Fluids* **20**, 086601.
- MILES, J. W. 1961 On the stability of heterogeneous shear flows. *J. Fluid Mech.* **10**, 496–508.
- ONU, K., FLYNN, M. R. & SUTHERLAND, B. R. 2003 Schlieren measurement of axisymmetric internal wave amplitudes. *Exp. Fluids* **35**, 24–31.
- PELIZ, A., LE CANN, B. & MOHN, C. 2009 Circulation and mixing in a deep submerged crater: tore seamount. *Geophys. Res. Abstr.* **11**, EGU2009–7567–1.
- SHMAKOVA, N., ERMANYUK, E. & FLÓR, J.-B. 2017 Generation of higher harmonic internal waves by oscillating spheroids. *Phys. Rev. Fluids* **2**, 114801.

- VLASENKO, V., STASHCHUK, N., INALL, M. E., PORTER, M. & ALEJNIK, D. 2016 Focusing of baroclinic tidal energy in a canyon. *J. Geophys. Res.* **121**, 2824–2840.
- VOISIN, B. 2003 Limit states of internal wave beams. *J. Fluid Mech.* **496**, 243–293.
- VOISIN, B., ERMANYUK, E. V. & FLÓR, J.-B. 2011 Internal wave generation by oscillation of a sphere, with application to internal tides. *J. Fluid Mech.* **666**, 308–357.